Sub-Micrometric MCM-41 Particles as Support to Design Efficient and Regenerable Maghemite-Based Sorbent for H₂S Removal

Claudio Cara[1, 2, 3], Elisabetta Rombi[1], Andrea Ardu[1, 2, 3], Mirko Antonio Vacca[1], and Carla Cannas[1, 2, 3, *]

[1]*Department of Chemical and Geological Sciences, University of Cagliari, Monserrato (CA), 09042, Italy*
[2]*Consorzio per la promozione di Attivitá Universitarie Sulcis-Iglesiente, Centro di Ricerca per l'Energia,*
l'Ambiente e il TErritorio, Palazzo Bellavista Monteponi, Iglesias (CI), 09016, Italy
[3]*Consorzio Interuniversitario Nazionale per la Scienza e Tecnologia dei Materiali (INSTM),*
Cagliari Unit, Via Giuseppe Giusti, 9, 50121, Firenze, Italy

In this work, highly dispersed maghemite (γ-Fe₂O₃) in form of ultrasmall nanoparticles (about 2 nm) was embedded into a mesostructured silica MCM-41 (about 600 nm) featuring regular sub-micrometric hexagonal shaped particles via the two-solvent incipient wetness impregnation strategy. The obtained nanocomposite was then tested as H₂S sorbent in the mid-temperature range. When compared with a commercial sorbent (Katalko$_{JM}$ 32-5), it showed superior performances after the first sulfidation which remained steady over three repeated sulfidation cycles, highlighting the regenerability properties of the composite. In order to evaluate the effect of the length of the pore channels on the accessibility of H₂S to the active phase, an analogous micrometric γ-Fe₂O₃@MCM-41, featuring micrometric channels and particles of irregular shape was used as reference.

Keywords: H₂S Removal, Sorbent, Mesostructured Silica, Maghemite.

1. INTRODUCTION

Iron oxides, due to their biocompatibility, non-toxicity, low cost,[1] combined with their magnetic[2] and semiconducting properties, have attracted great interest for several applications.[3–6] Among them, maghemite (γ-Fe₂O₃) with spinel structure, due to its ferrimagnetic properties and chemical stability, is widely used in different application fields, such as catalysis,[7, 8] biomedicine (magnetic resonance imaging (MRI),[9] drug delivery,[9, 10] and magnetic fluid hyperthermia (MFH),[11–13] gas sensor[14, 15] adsorption of liquid[16, 17] and gaseous pollutants.[18] Concerning this latter application, H₂S removal from natural gas and sour syngas is of particular interest considering the large amounts produced and the harmful effects on the environment, and damages on pipes and turbines caused by corrosion *phenomena* in industrial plants.[19–21] Among the several metal oxide-based candidates, although ZnO shows the most favorable thermodynamics, its main disadvantages such as the high regenerate temperature (at about 650 °C, depending on particle dimension and atmosphere composition),[19, 21, 22] and the moderate sulfur removal capacity per mass unit,[22, 27] render other oxides[20, 23, 24] like maghemite appealing substitutes.[18, 25, 26] In this context, maghemite has already proven itself to possess a remarkable ability to capture sulfur compounds,[18] with specific affinity for H₂S in a natural gas (CH₄) atmosphere,[27] due to the fast kinetics, the favorable thermodynamics of the reaction with H₂S,[26, 27] in a wide range of temperatures.[18, 29] However, even though the sulfidation process can be performed in the range of low temperature (<300 °C), avoiding in principle sintering or degradation *phenomena* of the sorbent, the regeneration process needs to be carried out above 350 °C,[18, 26] causing the gradual worsening in the sorbent's capacity. To overcome this issue, γ-Fe₂O₃ should be dispersed into a thermally stable support.[25, 26] Among the different supports, mesostructured silica shows ideal features to efficiently disperse the active phase. In fact, this strategy combines the distinctive features of mesostructured materials, such as high surface area and large accessibility owed to the regular dimension of the pores in the mesoporous range with the high H₂S removal capacity of maghemite,[18, 26] dispersed inside the pores in form of very small nanoparticles (with smaller dimension than the pore size).[26] The performance

---

*Author to whom correspondence should be addressed.

of the sorbents are strictly related to the active phase as well as to the textural proprieties of the silica support. In this framework, different supports showing different dimension of the pores (MCM-41 vs. SBA-15),[26] different silica particles dimension (from micrometric to nanometric particles),[26] and different porous structure (hexagonal *P6mm* and cubic *Ia3d*)[25] were used to obtain the corresponding efficient and regenerable γ-Fe$_2$O$_3$@SiO$_2$ sorbents for H$_2$S removal. Even though ultrasmall maghemite nanoparticles were obtained after the impregnation route in all the proposed supports, it was demonstrated that the best performances over repeated sulfidation-regeneration cycles were achieved with MCM-41 with micrometric particles, due to the high stability of the support. Therefore, the higher accessibility to the active phase that would be theoretically achieved when the silica particles are in the nanometric range, was not observed due to the collapse of the porous structure. However, the increase in the silica particle size, from the nanometric to the sub-micrometric scale, would permit to combine the high accessibility of nanometric particles and the high porous structure stability of the micrometric ones. In this work, sub-microsized mesostructured silica particles with regular hexagonal shape were efficiently synthesized using ethyl acetate to regulate the size and shape on the particles, and efficiently impregnated to obtain the corresponding γ-Fe$_2$O$_3$@MCM-41 composite by means of the two-solvent impregnation strategy. The resulting material was then tested as a H$_2$S sorbent at 300 °C over three repeated sulfidation-regeneration cycles, and the performances compared to those of a commercial sorbent and an analogous γ-Fe$_2$O$_3$-based sorbent obtained from microsized MCM-41 particles, prepared in the absence of ethyl acetate.[26]

2. EXPERIMENTAL DETAILS

2.1. Chemicals

All chemicals were of analytical grade and used as received without further purification. Hexadecyltrimethylammonium bromide (CTAB, 98%), ethanol (azeotropic 95.6%), ethyl acetate (EtOAc, 99.8%), ammonium hydroxide (NH$_4$OH, 28% NH$_3$ in H$_2$O), tetraethyl orthosilicate (TEOS, 98%), iron (III) nitrate nonahydrate (>99.5%), *n*-hexane (95%) were purchased from Sigma-Aldrich. Distilled water was used throughout the experiments.

2.2. MCM-41 Support Preparation

Sub-micrometric MCM-41 particles (MCM41_SM) were synthesized applying some modifications on the synthetic pathway presented in the reference articles.[26] Specifically, 1 g of CTAB was dissolved in 300 ml of distillate water and kept under mid stirring (300 rpm) for 1 hour at 30 °C. Then, 30 ml of NH$_4$OH and 5 ml of EtOAc were added and kept for 5 minutes under stirring. After that, the stirring rate was increased to 600 rpm and 5 ml of TEOS

were injected all at once into the solution. The resulting milky dispersion was kept for 2 hours under mid stirring (300 rpm). The consequent separation was performed by centrifugation, and the obtained white powder was washed three times using a mixture 1:1 of water:ethanol. After drying at 80 °C overnight, calcination was carry out at 550 °C for 4 hours (heating rate 2 °C min^{-1}) in order to remove the template.

2.3. Fe$_2$O$_3$@MCM-41 Sorbent Preparation

Mesostructured Fe$_2$O$_3$@MCM-41 composite featuring 10% w/w of Fe$_2$O$_3$ (actual loading 9.9% w/w) was prepared following the two-solvent incipient wetness impregnation.[30] In detail, 0.2 g of MCM41_SM were dried at 150 °C for two days to remove the adsorbed water from the pores and dispersed in 12 ml of hexane by stirring at 300 rpm at room temperature. After 2 hours of stirring, 177.8 μl (volume determined considering the total pore volume of the bare silica) of iron nitrate aqueous solution (1.551 M) were added dropwise and the suspension was kept under stirring for further 2 hours. Then, the temperature was increased to 80 °C to evaporate the hexane and a wet orange powder was obtained. After drying at 80 °C overnight, the resulting sample was calcined at 500 °C for 2 hours (eating rate 2 °C min^{-1}) to decompose the iron nitrate and obtain the corresponding iron oxide. The obtained sample was labelled Fe_MCM41_SM.

2.4. Characterization

Low-angle ($2\theta = 0.8°$–$2.5°$) and wide-angle ($2\theta = 10°$–$70°$) X-ray diffraction patterns were recorded on a Seifert instrument with a θ–θ geometry and a Cu Kα anode. The lattice parameter was calculated by the equation $a_0 = 2d_{100}/\sqrt{3}$. Textural analyses were carried out on a Micromeritics 2020 system by determining the nitrogen adsorption–desorption isotherm at -196 °C. Prior to analyses, the samples were heated for 24 hours under vacuum at 250 °C (heating rate, 1 °C $\cdot$ min^{-1}).

The Brunauer–Emmett–Teller (BET) specific surface area was calculated from the adsorption data in the P/P_0 range 0.05–0.17. The total pore volume was calculated at $P/P_0 = 0.99$, while the pore size distribution (PSD) was determined by applying the density functional theory (DFT) model (N$_2$-cylidrical pores-oxide surface) using the isotherm adsorption branch. The wall thickness was calculated as the difference between the lattice parameter (a_0) and the pore diameter (D_{pore}).

Transmission electron microscopy (TEM) images were obtained by means of JEOL200CX microscope operating at an accelerating voltage of 160 kV. Finely ground samples were dispersed in ethanol and sonicated, the suspensions were then dropped on carbon-coated copper grids. Particle size distribution was obtained by manual counting of the minor and major diameter of each particles using ImageJ software.

Dynamic Light Scattering (DLS) measurements were conducted by a Malvern Instrument Zeta Zetasized Ver 7.03, equipped with a He–Ne laser ($\lambda = 663$ nm, max 5 mW) and operating at a scattering angle of 173°. For these analyses, 2 mg of silica particles were dispersed in 2 mL of water and sonicated for 2 minutes. The dispersion was then transferred in a plastic cuvette and analyzed.

Room temperature (RT) ^{57}Fe Mössbauer spectra were measured in the transmission mode with ^{57}Co diffused into a Rh matrix as the source moving with constant acceleration. The spectrometer (Wissel) was calibrated by means of a standard α-Fe foil and the isomer shift was expressed with respect to this standard at room temperature. The fitting of the spectra was performed with the help of the NORMOS program using Lorentzian profiles.

2.5. Sulfidation and Regeneration Activity

To determine sulfidation and regeneration activity, 50 mg of iron oxide composite (Fe_MCM41_SM) were placed on a quartz wool bed (50 mg) and then in a vertical quartz tubular reactor coaxially located in an electrical furnace. Before sulfidation, a pre-treatment at 300 °C for 30 min under helium flow was performed to remove air and moisture from the sorbent and the reactor. Then, a reactant gas containing 15200 ppm of H_2S in helium (inlet flow, 20 cm^3 min^{-1}) was fed to the reactor and the H_2S content in the outlet flow during the sorption test was monitored by a quadrupole mass spectrometer (Thermo Electron Corporation). At the same time, H_2O and SO_2 signals were also monitored. Mass spectrometer calibration was carried out by recording the value of the electric signal of the H_2S species at different concentration, using gas cylinders of known H_2S concentration (100 ppm, 1000 ppm, 15200 ppm). Moreover, the less concentrated mixtures were diluted with He for obtaining calibration points from 33 to 104 ppm, i.e., lower or close to the breakthrough value (100 ppm). After fitting with the Weighted Function, the electric signal values were plotted as function of H_2S concentration. A linear correlation between the H_2S signal (eV) and the H_2S concentration (ppm) ($R = 0.99987$) was obtained. Standard deviation at 100 ppm was estimated to be 5 ppm.

Once reached 15200 ppm, the measure was stopped and the system was purged by flowing helium (20 cm^3 min^{-1}) for 1 hour. The amount of sulfur retained per unit mass of sorbent was determined when the outlet H_2S concentration attained 100 ppm by applying the formula:

$$\text{sulfur retention capacity (SRC)} = \frac{(F_s * B_t)}{W}$$

where F_s is the mass flow rate of sulfur (mg of S s^{-1}), B_t is the breakthrough time (s) and W is the sorbent weight (g), referring to the composite. The sulfur retention capacity of the sorbent was obtained as the difference between the B_t value of the composite and the B_t value

of the bare silica support. The error on the SRC values was estimated to be 2 mg$_S$ g$_{\text{sorbent}}^{-1}$ by carrying out several sulfidation cycles on fresh portions of the commercial sorbent Katalko$_{\text{JM}}$ 32-5. The regeneration process was performed on a Thermoquest 1100 TPD/R/O apparatus equipped with a thermal conductivity detector (TCD) and a quadrupole mass spectrometer (QMS) for monitoring SO_2 and O_2 signals. The composite was heated under air flow (20 cm^3 min^{-1}) up to 500 °C (heating rate, 10 °C min^{-1}) and the temperature was kept constant for 3 hours. To identify the sample after different sulfidation or regeneration runs, a letter (S or R, respectively) and a number (denoting successive runs) were added in the sample name.

3. RESULTS AND DISCUSSION

3.1. Fresh Sorbent Characterization

Figure 1(a) depicts low-angle XRD patterns of bare submicrosized MCM-41 (MCM41_SM) silica and corresponding composite (Fe_MCM41_SM). The presence of three reflections is clearly visible, ascribable to a hexagonal long-range mesoporous order (space group *P6mm*), proving that the impregnation route and the successive decomposition of the iron precursor have not given rise to any variation of the mesostructure. *d*-spacing and cell parameter (a_0) were calculated using the most intense reflection (100) and reported in Table I.

N_2 adsorption–desorption isotherms of the bare silica and the corresponding iron oxide composite are reported in Figure 1(b). According to IUPAC classification, both isotherms can be classify as IVB type[31] with an evident capillary condensation in the range 0.2–0.3. Textural parameters (surface area and pore volume), reported in Table I, highlight that the incorporation of the active phase has caused a decrease of about 16% and 22% in the surface area and pore volume values, respectively. DFT pore size distributions (Fig. 1(c)) point out that the symmetric distribution centred at 3.5 nm for MCM41_SM bare silica is shifted to lower values (3.3 nm) for the composite, due to the partial loading of the mesochannels by the iron oxide.

Wide-angle XRD patterns (Fig. 2(a)) reveal the presence in both the samples of a halo centred at 22°, related to amorphous silica, and two further weak and broad reflections at about 37° and 62°, due to the iron species, which appear only in the composite, indirectly proving that the iron species is highly dispersed in the silica mesochannels. In order to verify the nature of the iron-bearing phase, room temperature (RT) ^{57}Fe-Mössbauer spectroscopy was carried out (Fig. 2(b)). The spectrum shows a doublet with an isomer shift of 0.34 ± 0.01 mm s^{-1}, and a full width at half maximum (FWHM) of 0.47 ± 0.01 mm s^{-1}, indicating the formation of maghemite in form of ultrasmall nanoparticles.[2, 32–35] These values are very similar to those obtained in previous works for microsized γ-Fe$_2$O$_3$@MCM-41.[25, 26]
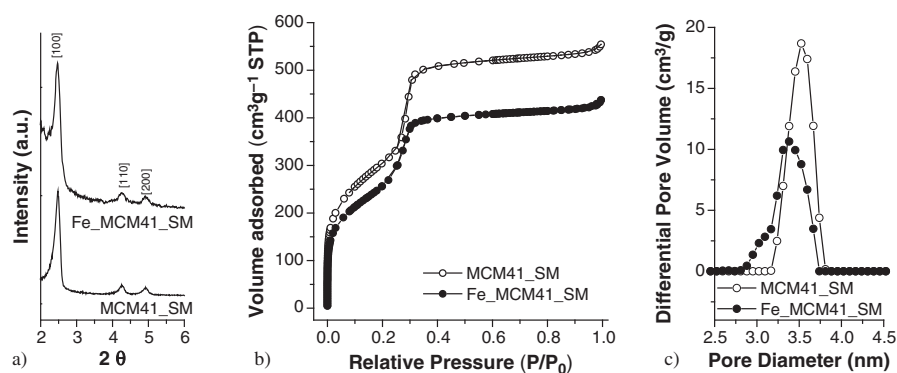
Figure 1. Low-angle XRD patterns (a) N_2-physisorption isotherms (b) and pore size distributions (c) of the MCM41_SM bare silica and the corresponding Fe_MCM41_SM composite.

Representative TEM images of MCM41_SM (Figs. 3(a, b)) show that the sample consists of particles having mainly hexagonal shape (Fig. 3(a)), with an average dimension of about 600 nm (570 ± 90 nm). Moreover, the high magnification image (Fig. 3(b)) reveals the existence of well-defined ordered channels with dimension of about 2–3 nm in all the particles, confirming low-angle XRD and pore size distribution data. The morphology and texture of the particles were retained even after the impregnation and calcination steps (Figs. 3(c, d)). Moreover, the appearance of dark spots and dark channels, spread all over the silica particles, proves that the iron oxide active phase was homogeneously embedded into/over the silica particles, with no evidence of iron oxide microcrystal formation. High magnification TEM image (Fig. 3(d)) gives evidence that the iron oxide particles are highly dispersed inside the pores in form of ultrasmall nanoparticles (smaller than pore dimensions, see black arrows).

DLS measurements confirm the TEM data, being the hydrodynamic diameter and dispersity (664 ± 130 nm) similar to the particle size and standard deviation determined from TEM (570 ± 90 nm) (Fig. 3(a), inset).

Table I. Textural features obtained by N_2-physisorption data for supports (MCM41_SM), composites (Fe_MCM41_SM, Fe_ MCM41_M) and three-time regenerated composites (Fe_MCM41_SM_3R, Fe_ MCM41_M_3R). S_{BET} = Surface area; V_p = Pore volume; D_p = pore diameter; w_t = walls thickness. Relative standard deviation: %RSD (S_{BET}) = 2.1%; %RSD (V_p) = 1.1%; %RSD (D_p) = 1.8%. d-spacing (d_{100}) and lattice parameter (a_0) obtained from the X-ray diffraction data.

Sample	S_{BET} (m^2g^{-1})	V_p (cm^3g^{-1})	D_p (nm)	w_t (nm)	d_{100}	a_0
MCM41_SM	1111	0.86	3.5	0.6	3.6	4.1
Fe_MCM41_SM	927	0.67	3.3	0.8	3.6	4.1
Fe_MCM41_SM_3R	756	0.53	3.3	0.8	3.6	4.1
Fe_MCM41_M*	768	0.53	3.2	0.8	3.5	4.0
Fe_MCM41_M_3R*	771	0.49	3.1	0.8	3.4	3.9

Note: *Textural values reported in the referenced articles.[26]

TEM allows to verify the role of ethyl acetate in regulating size and shape of the support's particles. In fact, the MCM41_M sample, prepared in the same conditions of MCM41_SM, but in the absence of ethyl acetate, shows mesostructured micrometric particles with irregular shape and very broad particle size distribution (Figs. 3(e, f)). The limited growth of the particle size and the shape regulation observed upon addition of ethyl acetate in the aqueous reaction mixture can be most probably ascribed to a decrease in the pH, due to the formation of acetic acid.[26, 36] The effect of ethyl acetate, already demonstrated for mesostructured silica in form of nanoparticles (70–200 nm),[26, 36] has been proven here also for sub-micrometric ones.

3.2. Sulfidation and Regeneration Processes

To evaluate the H_2S removal performance of the Fe_MCM41_SM composite, three sulfidation runs have been carried out at mid-temperature (300 °C). After each sulfidation, a regeneration step has been performed by heating the sample under air flow up to 500 °C, in order
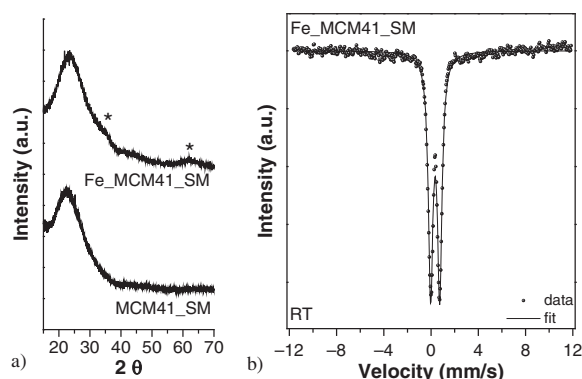
Figure 2. Wide-angle XRD patterns of MCM41_SM pure silica and corresponding Fe_MCM41_SM composite featuring 10% w/w of iron oxide active phase (a); RT ^{57}Fe-Mössbauer spectrum of the Fe_MCM41_SM composite (b).
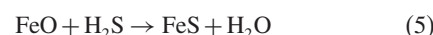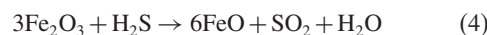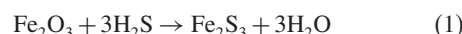
MCM41_SM
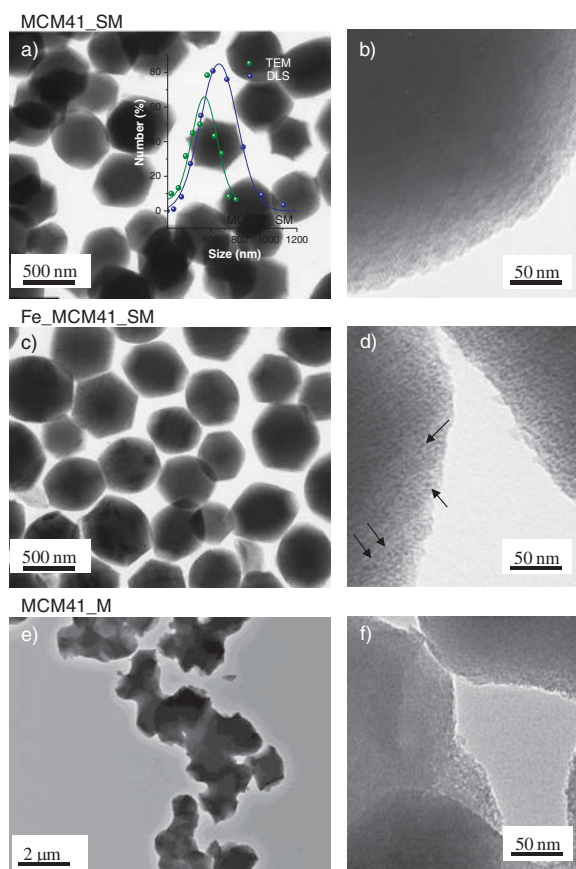
Fe_MCM41_SM

MCM41_M

Figure 3. Bright field images at different magnification of MCM41_SM (a, b), and corresponding Fe_MCM41_SM composite (c, d). Inset in (a) shows the particles size distribution of MCM41_SM, determined by both dynamic light scattering and TEM images. Bright field images of the microsized MCM41_M support are also reported for comparison (e, f).

to regenerate the iron oxide phase. The sulfur retention capacities (SRC) for each sulfidation run have been listed in Table II and compared with the ones obtained for Fe_MCM41_M composite, built up with micrometric silica particles, and with those obtained for a commercial non-supported ZnO sorbent (Katalko$_{JM}$ 32-5). Fe_MCM41_SM shows fairly lower SRC values compared with Fe_MCM41_M, but higher values than Katalko$_{JM}$ 32-5 after the first sulfidation-regeneration cycle.

Figure 4(a) reports the H$_2$S profiles during the three sulfidation runs of the Fe_MCM41_SM sorbent, in which it is possible to evince the breakthrough time at 100 ppm of H$_2$S, used to determine the corresponding SRC values. The obtained values result to be very similar for the three sulfidation runs, with no evidence of decline after the regeneration steps. However, it should be noted from Figure 4(a) that, for run times beyond the breakthrough one, the profiles of H$_2$S released during the first and the successive sulfidation tests are very different, a much steeper increase being observed for the latter. Therefore, moving the H$_2$S

limit concentration from 100 ppm to, e.g., 400 ppm, a clear enhancement of the performance of the fresh sorbent is observable (SRC = 30 mg$_S$ g$_{sorbent}^{-1}$), in comparison with that of the regenerated ones, which show a SRC value of 17 ± 1 mg$_S$ g$_{sorbent}^{-1}$.

To verify the possible reactions involved during the sulfidation process, the release of different species, such as H$_2$O and SO$_2$ were also monitored, and the corresponding profiles during the first sulfidation run are reported in Figure 4(b) together with that of H$_2$S. It can be observed from the figure that the retention of H$_2$S is accompanied by a significant release of H$_2$O and by a very small amount of SO$_2$. Considering these results, it can be suggested that the sulfidation process is largely governed by a substitution reaction, according to the Eqs. (1)–(3),[25, 26] though the oxidation-reduction reaction between Fe^{III} and H$_2$S cannot be completely neglected, as confirmed by SO$_2$ formation (Eqs. (4)–(5)).[25, 26]

$$Fe_2O_3 + 3H_2S \rightarrow Fe_2S_3 + 3H_2O \quad (1)$$

$$2Fe_2S_3 \rightarrow FeS_2 + Fe_3S_4 \quad (2)$$

$$Fe_2S_3 \rightarrow \alpha FeS_2 + \beta FeS_x + \gamma S \quad (3)$$

$$3Fe_2O_3 + H_2S \rightarrow 6FeO + SO_2 + H_2O \quad (4)$$

$$FeO + H_2S \rightarrow FeS + H_2O \quad (5)$$

The regeneration process has been monitored following the composition of the gas released by both a Thermal Conductivity Detector (TCD) and a Quadrupole mass spectrometer (Fig. 4(c)). TCD profile (green line in the graph) shows the presence of two peaks centred at 255 °C and 302 °C, both ascribable to oxygen consumption, as confirmed by the QMS signals of O$_2$ (orange line). Moreover, an additional large band associated with SO$_2$ release has also been detected, as confirmed by the QMS signals of SO$_2$ (black line). Considering the whole regeneration profile, the oxygen consumption can be relatedto the presence

Table II. Breakthrough time (B_t) and sulfur retention capacity (SRC) of fresh and regenerated iron oxide-based sorbents (Fe_MCM41_SM, Fe_MCM41_M) and unsupported sorbent (Katalko$_{JM}$ 32-5). R1 is referred to the regenerated sample after one sulfidation and consecutive regeneration, R2 to the regenerated sample after two sulfidation-regeneration cycles, R3 to the regenerated sample after three sulfidation-regeneration cycles. The error in the SRC value is estimated to be ± 2 mg$_S$ g$_{sorbent}^{-1}$.

Sample	Sulfidation run	B_t (s)	SRC (mg$_S$ g$_{sorbent}^{-1}$)
Fe_MCM41_SM	1st	98	13
Fe_MCM41_SM_R1	2nd	107	14
Fe_MCM41_SM_R2	3rd	99	13
Fe_MCM41_M*	1st	295	38
Fe_MCM41_M_R1	2nd	169	22
Fe_MCM41_M_R2	3rd	169	22
Katalko$_{JM}$ 32-5*	1st	122	16
Katalko$_{JM}$ 32-5_R1	2nd	10	1
Katalko$_{JM}$ 32-5_R2	3rd	13	2

*Note*: *SRC value present in the referenced article.[26]
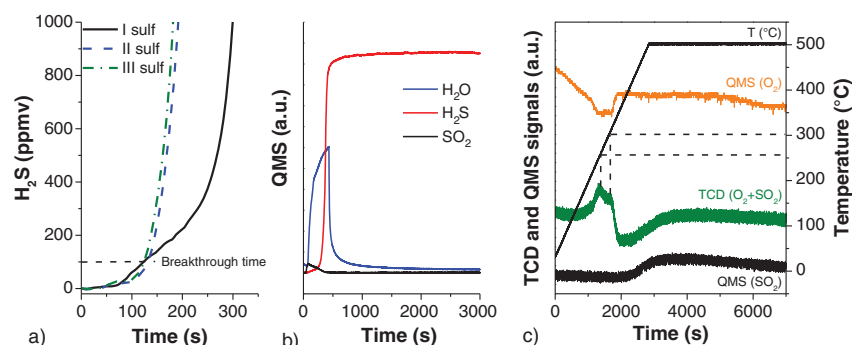
Figure 4. H$_2$S profiles during the sulfidation processes (sulf: Sulfidation) (a); H$_2$S, SO$_2$ and H$_2$O breakthrough curves of the Fe_MCM41_SM during the first sulfidation run (b); TCD profile and SO$_2$ and O$_2$ Quadrupole Mass Spectrometer (QMS) signals of Fe_MCM41_SM during the first regeneration run.

of a sulfided iron phase, from which the iron oxide phase is restored by reaction with oxygen and consequent release of SO$_2$.

3.3. Regenerated Sorbent Characterization

After three sulfidation-regeneration cycles, the sub-microsized sorbent (Fe_MCM41_SM_3R) has been characterized by low-angle XRD and N$_2$-physisorption measurements (Figs. 5(a–c)) to verify the porous structure stability, compared to the fresh (Fe_MCM41_SM) and the microsized ones (Fe_MCM41_M and Fe_MCM41_M_3R). The mesostructure is retained, as confirmed by the presence of well-defined reflections in the low-angle XRD pattern of Fe_MCM41_SM_3R.
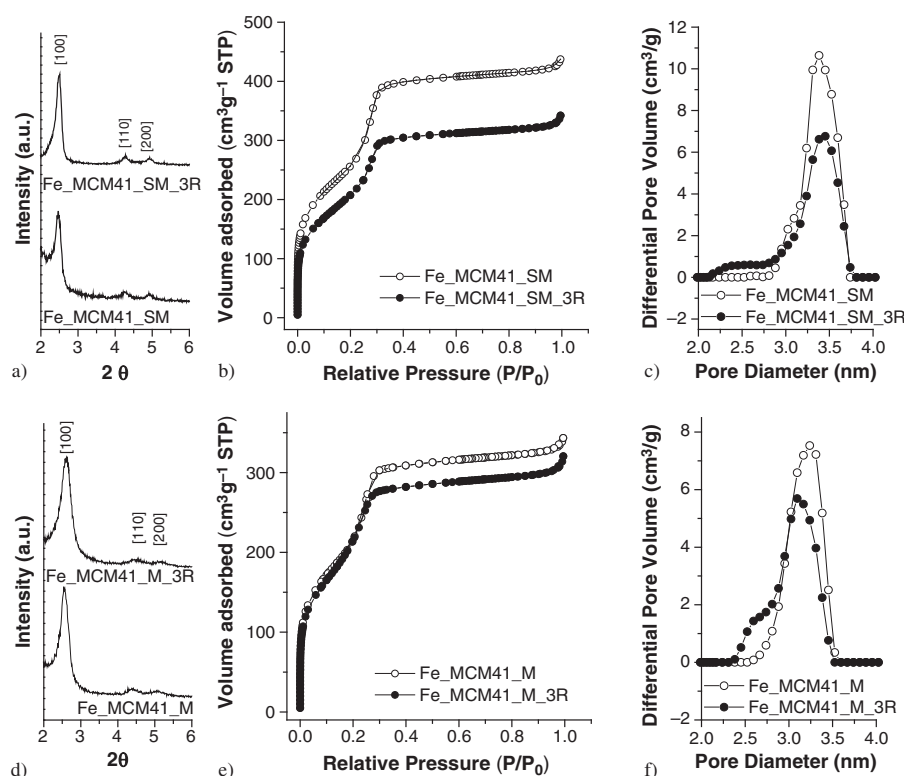
Figure 5. Low-angle XRD patterns, N$_2$-physisorption isotherms and DFT pore size distributions of: Fresh Fe_MCM41_SM, and corresponding three-time sulfidated-regenerated Fe_MCM41_SM_3R composite (a–c); fresh Fe_MCM41_M and corresponding three-time sulfidated-regenerated Fe_MCM41_M_3R composite (d–f). (d) and (e) Reproduced with permission from [26], C. Cara, et al., *J. Mater. Chem. A* 5, 41 (**2017**).

N_2 adsorption–desorption isotherms give a similar information, even though a gradual reduction in the surface area (from 927 to 756 m^2g^{-1}, almost 18% less) and pore volume (from 0.67 to 0.53 cm^3g^{-1}) is evidenced (see Table I). DFT analysis reveals the appearance of a new contribution at lower pore size values in the PSD curve of the Fe_MCM41_SM_3R sample (Fig. 5(c)), indicating that the repeated sulfidation-regeneration cycles cause a reduction in the diameter of a portion of mesopores. The retention of the porous structure (Fig. 5(d)) as well as the presence of the contribution at lower pore size values (Fig. 5(f)) can also be observed for the analogous Fe_MCM41_M_3R with micrometric size. However, at variance with Fe_MCM41_SM_3R, surface area and pore volume of the micrometric composite result unchanged after the sulfidation-regeneration cycles (see Table I).

According to the literature, the collapse of the porous structure in mesostructured silica systems can be related to the hydrolysis of siloxane bridges at the surface to form silanol groups.[37] Taking into account the role of ethyl acetate as growth inhibitor and shape regulator, the differences in the structural stability of Fe_MCM41_SM and Fe_MCM41_M could be reasonably ascribed to its effect on the concentration and nature of the surface silanol groups. A partial collapse of the pore structure has been also revealed, even more pronounced, for nanosized MCM-41 particles, synthesized using a higher amounts of ethyl acetate.[25, 38] As a consequence, a gradual covering of a portion of the active phase takes place, hampering the reaction of such iron oxide nanoparticles with H_2S, affecting the H_2S removal performance in the successive cycles. Therefore, the reduction in the size of the mesostructured support particles from micrometric (Fe_MCM41_M) to sub-micrometric (Fe_MCM41_SM) does not cause the expected enhancement in terms of sulfur retention capacity; on the contrary, a partial decline of the SRC performances was observed. Excluding the differences between the two composites in the first sulfidation, due to the possible occurrence of other *phenomena*, (such as adsorbed water, no complete crystallization of the active phase, stabilization of the porous structure in the test conditions)[25] the comparison of the SRC values in the successive sulfidation cycles highlights that the high stability of the porous structure of the microsized composite plays a key role in guaranteeing high H_2S removal performances (67% higher than for the sub-microsized one). Therefore, the present results, while confirming the remarkable size and shape-regulating effect of ethyl acetate, clearly show its detrimental influence on the porous structure stability and the performance of the related sorbent.

4. CONCLUSION

γ-Fe_2O_3@MCM-41 composites have already been proved to be promising sorbents for H_2S adsorption in the mid-temperature range. Furthermore, it was demonstrated that the dimension of the silica particles used as support plays a strategic role in the performance of the sorbent: while micrometric silica particles obtained in the absence of a regulating agent (ethyl acetate) are highly stable over the repeated sulfidation-regeneration cycles, a partial collapse of the silica structure occurred in the case of nanometric ones, causing detrimental effects on H_2S removal performances. Here, with the ambition of joining the high accessibility to the iron oxide active phase embedded in silica nanoparticles, owing to its short pore channels, with the high thermal stability of the pore structure shown by the micrometric systems, sub-micrometric silica particles were synthesized and employed to homogeneously disperse γ-Fe_2O_3 ultrasmall nanoparticles. The H_2S removal performances of the resulting sorbent (Fe_MCM41_SM) over three repeated sulfidation cycles were then compared with those of the micrometric sample (Fe_MCM41_M). Even though the H_2S removal capacities of Fe_MCM41_SM are stable and much higher than those of the commercial sorbent after the first sulfidation, they are lower than those of the micrometric Fe_MCM41_M. The textural characterization of the sorbents after the repeated cycles reveals that the reduction of the silica particle dimension causes a detrimental effect on the H_2S removal performances, due to the partial collapse of the structure. However, in the light of the similar H_2S profiles of Fe_MCM41_SM after the first sulfidation, it seems that the porous structure of the regenerated sorbent remains stable, enabling a steady performance over the course of different sulfidation processes.

References and Notes

1. A. Hervault and N. T. K. Thanh, *Nanoscale* 6, 20 (**2014**).
2. R. M. Cornell and U. Schwertmann, The Iron Oxides, FRG: Wiley-VCH Verlag GmbH & Co. KGaA, Weinheim (**2003**).
3. K. Sivula, F. Le Formal, and M. Grätzel, *ChemSusChem* 4, 4 (**2011**).
4. M. C. Pereira, L. C. A. Oliveira, and E. Murad, *Clay Miner* 47, 3 (**2012**).
5. Q. Hao, L. Li, X. Yin, S. Liu, Q. Li, and T. Wang, *Mater. Sci. Eng. B Solid-State Mater. Adv. Technol.* 176, 7 (**2011**).
6. H. Chen, Y. Zhao, M. Yang, J. He, P. K. Chu, J. Zhang, and S. Wu, *Anal. Chim. Acta* 659, 1 (**2010**).
7. A. K. Dutta, S. K. Maji, and B. Adhikary, *Mater. Res. Bull.* 49, 1 (**2014**).

 8. M. B. Gawande, P. S. Branco, and R. S. Varma, *Chem. Soc. Rev.* 42, 8 (**2013**).
 9. N. Nasongkla, E. Bey, J. Ren, H. Ai, C. Khemtong, J. S. Guthi, S.-F. Chin, A. D. Sherry, D. A. Boothman, and J. Gao, *Nano Lett.* 6, 11 (**2006**).
10. M. Arruebo, R. Fernández-Pacheco, M. R. Ibarra, and J. Santamaría, *Nano Today* 2, 3 (**2007**).
11. V. Mameli, A. Musinu, A. Ardu, G. Ennas, D. Peddis, D. Niznansky, C. Sangregorio, C. Innocenti, N. T. K. Thanh, and C. Cannas, *Nanoscale* 8, 19 (**2016**).
12. A. K. Gupta and M. Gupta, *Biomaterials* 26, 18 (**2005**).
13. C. S. S. R. Kumar and F. Mohammad, *Adv. Drug Deliv. Rev.* 63, 9 (**2011**).
14. K. Movlaee, M. Ganjali, P. Norouzi, and G. Neri, *Nanomaterials* 7, 12 (**2017**).
15. F. G. de Souza, J. A. Marins, J. C. Pinto, G. E. de Oliveira, C. M. Rodrigues, and L. M. T. R. Lima, *J. Mater. Sci.* 45, 18 (**2010**).
16. X. Peng, Y. Zhao, T. Yang, Y. Yang, Y. Jiang, Z. Ma, X. Li, J. Hou, B. Xi, and H. Liu, *Microporous Mesoporous Mater.* 258, 26 (**2018**).
17. P. N. Dave and L. V. Chopda, *J. Nanotechnol.* 2014, 1 (**2014**).
18. G. Huang, E. He, Z. Wang, H. Fan, J. Shangguan, E. Croiset, and Z. Chen, *Ind. Eng. Chem. Res.* 54, 34 (**2015**).
19. M. Wu, L. Shi, T. T. Lim, A. Veksha, F. Yu, H. Fan, and J. Mi, *Chem. Eng. J.* 353, 273 (**2018**).
20. M. Wu, T. Li, H. Li, H. Fan, and J. Mi, *Energy and Fuels* 31, 12 (**2017**).
21. M. Wu, L. Jia, H. Fan, and J. Mi, *Energy Fuels* 31, 9 (**2017**).
22. M. Mureddu, I. Ferino, E. Rombi, M. G. Cutrufello, P. Deiana, A. Ardu, A. Musinu, G. Piccaluga, and C. Cannas, *Fuel* 102, 691 (**2012**).
23. B. Elyassi, Y. Al Wahedi, N. Rajabbeigi, P. Kumar, J. S. Jeong, X. Zhang, P. Kumar, V. V Balasubramanian, M. S. Katsiotis, K. Andre Mkhoyan, N. Boukos, S. Al Hashimi, and M. Tsapatsis, *Microporous Mesoporous Mater.* 190, 152 (**2014**).
24. M. Behl, J. Yeom, Q. Lineberry, P. K. Jain, and M. A. Shannon, *Nat. Nanotechnol.* 7, 12 (**2012**).
25. C. Cara, E. Rombi, V. Mameli, A. Ardu, M. S. Angotzi, D. Niznansky, A. Musinu, and C. Cannas, *J. Phys. Chem. C* 122, 23 (**2018**).
26. C. Cara, E. Rombi, A. Musinu, V. Mameli, A. Ardu, M. S. Angotzi, L. Atzori, D. Niznansky, H. L. Xin, and C. Cannas, *J. Mater. Chem. A* 5, 41 (**2017**).
27. M. S. Shah, M. Tsapatsis, and J. I. Siepmann, *Chem. Rev.* 117, 14 (**2017**).
28. M. Mureddu, I. Ferino, A. Musinu, A. Ardu, E. Rombi, M. G. Cutrufello, P. Deiana, M. Fantauzzi, and C. Cannas, *J. Mater. Chem. A* 2, 45 (**2014**).
29. S. C. Tseng, S. S. Tamhankar, and C. Y. Wen, *Chem. Eng. Sci.* 36, 8 (**1981**).
30. J. Van Der Meer, I. Bardez-Giboire, C. Mercier, B. Revel, A. Davidson, and R. Denoyel, *J. Phy. Chem. C* 114, 8 (**2010**).
31. M. Thommes, K. Kaneko, A. V. Neimark, J. P. Olivier, F. Rodriguez-Reinoso, J. Rouquerol, and K. S. W. Sing, *Pure Appl. Chem.* 87, 9 (**2015**).
32. F. Bødker, M. F. Hansen, and C. B. Koch, *Matter Mater. Phys.* 61, 10 (**2000**).
33. F. Bødker and S. Mørup, *Europhys. Lett.* 52, 2 (**2000**).
34. G. Muscas, G. Concas, C. Cannas, A. Musinu, A. Ardu, F. Orrù, D. Fiorani, S. Laureti, D. Rinaldi, G. Piccaluga, and D. Peddis, *J. Phys. Chem. C* 117, 44 (**2013**).
35. V. Mameli, A. Musinu, D. Niznansky, D. Peddis, G. Ennas, A. Ardu, C. Lugliè, and C. Cannas, *J. Phys. Chem. C* 120, 48 (**2016**).
36. T. Suteewong, H. Sai, R. Cohen, S. Wang, M. Bradbury, B. Baird, S. M. Gruner, and U. Wiesner, *J. Am. Chem. Soc.* 133, 2 (**2011**).
37. M. Varache, I. Bezverkhyy, F. Bouyer, R. Chassagnon, F. Baras, and F. Bouyer, *J. Nanoparticle Res.* 17, 9 (**2015**).
38. C. M. Carbonaro, F. Orrù, P. C. Ricci, A. Ardu, R. Corpino, D. Chiriu, F. Angius, A. Mura, and C. Cannas, *Microporous Mesoporous Mater.* 225, 432 (**2016**).